Enhance seasonal amplitude of atmospheric CO2 by the changing Southern Ocean carbon sink

Jeongmin Yun, Sujong Jeong, Nicolas Gruber, Luke Gregor, Chang Hoi Ho, Shilong Piao, Philippe Ciais, David S. Schimel, Eun-Young Kwon

ATMOSPHERIC SCIENCE

Enhance seasonal amplitude of atmospheric CO_2 by the changing Southern Ocean carbon sink

Jeongmin Yun[1,2]†, Sujong Jeong[1,2]*†, Nicolas Gruber[3], Luke Gregor[3], Chang-Hoi Ho[4], Shilong Piao[5,6], Philippe Ciais[7], David Schimel[8], Eun Young Kwon[9,10]

The enhanced seasonal amplitude of atmospheric CO_2 has been viewed so far primarily as a Northern Hemisphere phenomenon. Yet, analyses of atmospheric CO_2 records from 49 stations between 1980 and 2018 reveal substantial trends and variations in this amplitude globally. While no significant trends can be discerned before 2000 in most places, strong positive trends emerge after 2000 in the southern high latitudes. Using factorial simulations with an atmospheric transport model and analyses of surface ocean Pco_2 observations, we show that the increase is best explained by the onset of increasing seasonality of air-sea CO_2 exchange over the Southern Ocean around 2000. Underlying these changes is the long-term ocean acidification trend that tends to enhance the seasonality of the air-sea fluxes, but this trend is modified by the decadal variability of the Southern Ocean carbon sink. The seasonal variations of atmospheric CO_2 thus emerge as a sensitive recorder of the variations of the Southern Ocean carbon sink.

INTRODUCTION

The global carbon cycle is changing rapidly in response to human-caused emissions, as conspicuously evidenced by the long-term increase in atmospheric CO_2 (*1*). A remarkable feature in this record is that as atmospheric CO_2 is rising, its seasonal amplitude (AMP) is increasing as well (*2*, *3*). Since the seasonality of fossil fuel emissions is small (*4*), the variations of AMP primarily reflect a changing imbalance between uptake and release of CO_2 by terrestrial ecosystems (e.g., photosynthesis versus respiration) and by the oceans (e.g., biological versus solubility pumps). The increase of AMP was first noted in the 1990s from long-term surface atmospheric CO_2 measurements in the Northern Hemisphere (NH) (*2*) and later ascribed to flux changes in the northern high latitudes from surface records and early aircraft observations (*5*). This signal was attributed to changes in terrestrial fluxes, including enhanced photosynthesis (*5*–*10*), accelerated decomposition of soil organic matter (*7*, *11*), and greater cropland production (*12*, *13*).

When studying AMP trends in the NH, the ocean plays a small role compared to the land. By contrast, AMP in the Southern Hemisphere (SH) is sensitive to changes in the Southern Ocean (*14*–*16*). Of particular interest is the imprint of the decadal changes in the Southern Ocean carbon sink on atmospheric CO_2, especially its AMP. Model simulations (*17*, *18*) and observation-based analyses have suggested that the Southern Ocean carbon sink weakened in the 1990s but reinvigorated after the turn of the millennium (*18*–*20*). This leads not only to changes in the meridional gradient in atmospheric CO_2 (*16*) but also potentially to an increase in the AMP. This effect may enhance an underlying trend in the seasonality of the air-sea CO_2 fluxes caused by ocean acidification (*21*–*23*).

In this study, we revisit the trends of AMP, especially those in the SH, by reanalyzing atmospheric records from 49 surface stations across all the latitudes during the period 1980–2018. The potential mechanisms underlying the AMP trends are explored via factorial simulations with an atmospheric transport model and via air-sea CO_2 flux products based on observations of the surface ocean CO_2 partial pressure (Pco_2).

RESULTS

Trends in seasonal amplitude of atmospheric CO_2

Over the past four decades (1980–2018), long-term global atmospheric CO_2 measurements show that AMP, here measured as the value of annual maximum minus minimum, has increased rapidly in the Arctic [0.94 ppm decade^{-1} for Barrow (BRW)], moderately in tropical and subtropical NH regions [0.18 ppm decade^{-1} for Mauna Loa (MLO)], and weakly in the SH [0.03 ppm decade^{-1} for South Pole (SPO)] (fig. S1). Zonally averaged AMP estimated from inverse modeling (*24*, *25*) confirms these latitudinal features of the AMP trends. A more detailed analysis of these trends using 20-year moving windows reveals that for most of the 49 investigated sites, the long-term (1980–2018) trends in AMP are primarily caused by the period after 2000, while the trends are, with the exception of BRW, statistically insignificant or even negative for the periods before 2000 (Fig. 1, A and B). For the period 2000–2018, we find positive trends of AMP in the tropics (0° to 25°) and south of 45°S, while the trends are insignificant between 25°S and 45°S (Fig. 1A). Although the post-2000 AMP change south of 45°S (0.21 [0.17, 0.25] ppm decade^{-1}: mean [95% confidence intervals]; 1000 bootstrap samples) is modest in absolute size, it corresponds to a +29% [24, 36%] increase in its climatological value (fig. S2).

The finding of substantial changes in the AMP trends around the turn of the millennium is confirmed by the presence of significant breakpoints in AMP detected in 2000 and 1999, respectively, at

[1]Department of Environmental Planning, Graduate School of Environmental Studies, Seoul National University, Seoul, Republic of Korea. [2]Environmental Planning Institute, Seoul National University, Seoul, Republic of Korea. [3]Environmental Physics, Institute of Biogeochemistry and Pollutant Dynamics, ETH Zurich, Zurich, Switzerland. [4]School of Earth and Environmental Sciences, Seoul National University, Seoul, Republic of Korea. [5]Sino-French Institute for Earth System Science, College of Urban and Environmental Sciences, Peking University, Beijing, China. [6]Key Laboratory of Alpine Ecology and Biodiversity, Institute of Tibetan Plateau Research, Chinese Academy of Sciences, Beijing, China. [7]Laboratoire des Sciences du Climat et de l'Environnement, CEA CNRS UVSQ, Gif-sur-Yvette, France. [8]Jet Propulsion Laboratory, California Institute of Technology, Pasadena, CA 91101, USA. [9]Center for Climate Physics, Institute for Basic Science, Busan, Republic of Korea. [10]Pusan National University, Busan, Republic of Korea.
*Corresponding author. Email: sujong@snu.ac.kr
†These authors contributed equally to this work.

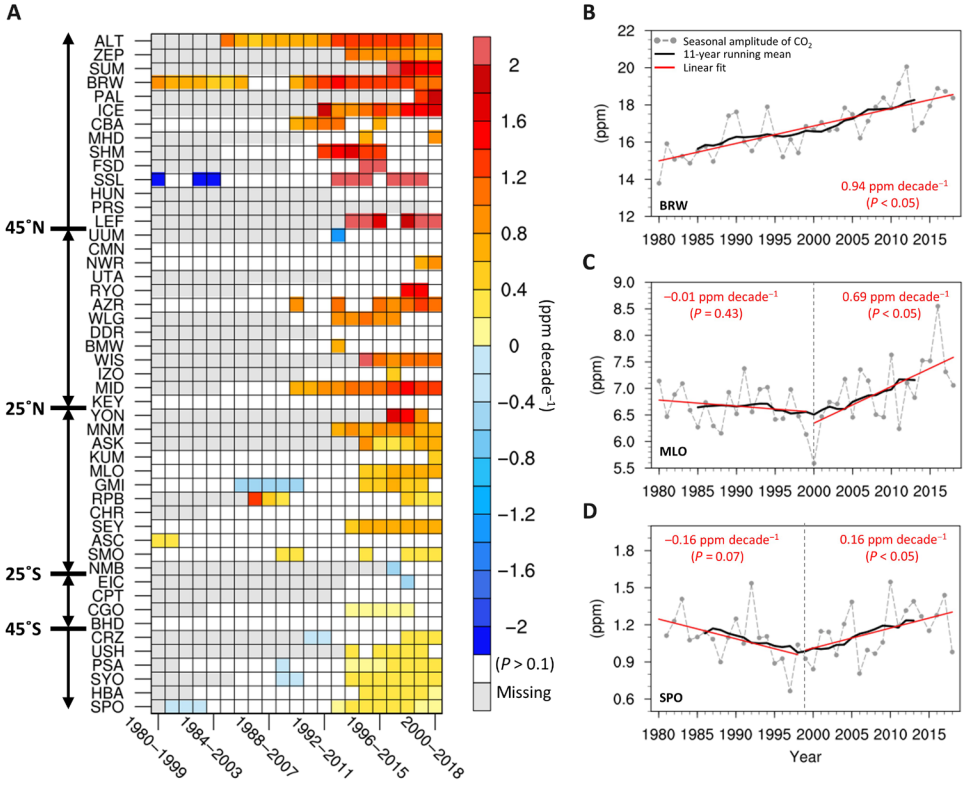

Fig. 1. Changes in trends of seasonal amplitude of atmospheric CO_2 (AMP). (**A**) Twenty-year (19-year for last period) moving trends of observed AMP at 45 stations. White and colored grids indicate nonsignificant trends ($P > 0.1$, two-tailed Student's t test) and significant trends ($P < 0.1$), respectively. Ash-colored grids denote missing data. Station abbreviations are defined in table S1. (**B** to **D**) Time series of observed AMP at (B) BRW (71.3°N, 156.6°W), (C) MLO (19.5°N, 155.6°W), and (D) SPO (90°S, 24.8°W) observatories. Thick black line represents 11-year running averaged AMP, and red line represents linear fit of AMP before and after its breakpoint. Segmented regression lines are plotted when the regression coefficients before and after the breakpoint are significantly different ($P < 0.05$); otherwise, a single regression line is drawn.

the two sites with the longest records, i.e., MLO and SPO. At MLO, the AMP trend from 1980 to 1999 was statistically insignificant ($P = 0.43$) (Fig. 1C), but after 2000, it increased to 0.69 ppm decade^{-1} ($P < 0.05$). A similar break occurred at SPO, where the trend is even negative before 1998 (0.16 ppm decade^{-1}; $P = 0.07$) but then increased to 0.16 ppm decade^{-1} ($P < 0.05$) after 1999 (Fig. 1D). This change in AMP trends prevails over all but one [Ushuaia (USH) Station] analyzed station south of 45°S (Fig. 1A and fig. S2), although the stronger seasonal cycle and the higher interannual variability of atmospheric CO_2 at these sites closer to the Southern Ocean make the changes in AMP less conspicuous than those at SPO that is quite remote from this major source of flux variability (e.g., fig. S3). For example, the application of the segmented regression model to the record from Palmer Station Antarctica (PSA) reveals the same increasing trend for the 1999–2018 period (0.22 ppm decade^{-1}; $P < 0.05$) as seen at SPO, but the breakpoint is not significant (fig. S4).

Changes in surface CO_2 fluxes

The primary process altering the AMP is the net sources and sinks of CO_2 at the Earth's surface, i.e., changes in the seasonality of the fossil fuel emissions, or in the sources and sinks of the terrestrial biosphere or the ocean. While the AMP increases at northern high latitudes are attributed primarily to changes in the terrestrial biosphere [(*5*–*11*); also see Fig. 2A], the changes in AMP in the SH and particularly in its high latitudes must be driven primarily by the ocean. This is because the seasonality of tropical biomes and the fraction of land area in the southern high latitudes are much smaller and also because of the comparably small impact of fossil fuel emissions on atmospheric CO_2 variations in the SH (*14*, *16*).

The impact of the ocean on the seasonality of atmospheric CO_2 has been given little attention so far. One reason is the generally lower flux density of the air-sea fluxes compared to the exchange fluxes with the terrestrial biosphere (*26*). Another reason is that the seasonality of the CO_2 exchange with the ocean reverses between the low and high latitudes (*22*, *27*). In the high latitudes (poleward of 40° latitude), the ocean acts as a sink in summer (i.e., boreal in the NH and austral in the SH) and as a source in winter (i.e., the seasonality of the air-sea flux in the high latitudes is in sync with that of the terrestrial flux) (Fig. 2A). In contrast, in the low latitudes (10° to 40°), with the ocean acting as a source in summer and a sink in winter, the seasonality of the air-sea flux is opposite to that of the terrestrial flux.

The observed increase in the seasonality of pCO_2 (*22*), which acts as the main thermodynamic driving force for the exchange of CO_2 across the air-sea interface (*27*), thus causes opposing effects in the AMP between the low and high latitudes. It tends to enhance the AMP in the high latitudes but dampens it in the low latitudes. By using the observational product of (*28*) that underlies the work of (*22*) and four additional observation-based pCO_2 products (*29*–*32*), we found that seasonal differences in pCO_2, calculated as the absolute value of the winter minus summer differences, have significantly increased during 2000–2018 in all regions by more than 2.5 μatm decade^{-1}

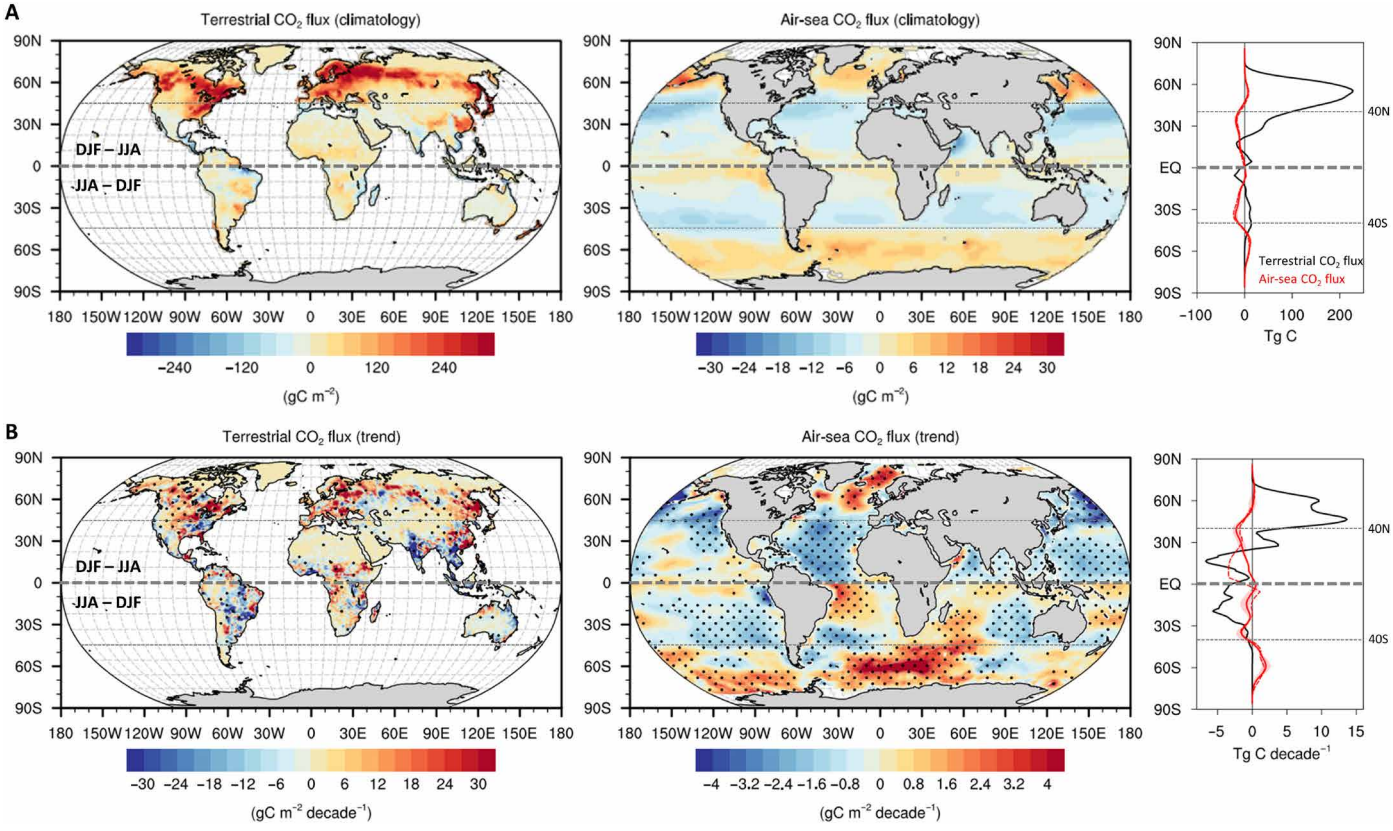

Fig. 2. Spatial distribution of mean and trends of seasonal differences in CO_2 fluxes. Spatial distribution of (**A**) climatology and (**B**) annual trend of differences in terrestrial and air-sea CO_2 fluxes between summer and winter (winter minus summer with positive denoting fluxes into the atmosphere) for 2000–2018 (2016 for terrestrial fluxes). The stippled areas represent statistically significant annual trends ($P < 0.05$, two-tailed Student's t test). Right-hand panels show their zonally integrated latitudinal distribution smoothed by 10° moving average. Terrestrial CO_2 fluxes are simulated from Community Land Model 4.5, and air-sea CO_2 fluxes (black line) are derived from an inverse modeling (CAMS; dotted red line) and five observation-based pCO_2 data products (OceanSODA-ETHZ, Jena-MLS, MPI-SOMFFN, CSIR-ML6, and CMEMS-FFNN; solid red line). The red shaded areas represent the 95% confidence intervals derived from 1000 bootstrap samples of datasets.

except in the southern low latitudes (0.7 [0.1, 1.6] μatm decade^{-1}) where the data-driven estimates are inconsistent (fig. S5B). Qualitatively, this fits well with the observed AMP changes in the SH: the nonsignificant trends in low latitudes and significant increases in high latitudes after 2000. Together, this finding is also confirmed by the estimates of trends in seasonal differences of air-sea flux derived from these pCO_2 products and inverse modeling (*24*), indicating more than five times greater increases in high latitudes than in low latitudes in the SH (Fig. 2B). Moreover, in the southern high latitudes, the absence of a significant trend in the AMP before 2000 is consistent with a much lower to nearly absent trend in the seasonal difference in pCO_2 during 1986–1999, but the high inconsistency (−0.3 [−2.0, 1.4] μatm decade^{-1}), likely emanating from the sparser measurements, makes this conclusion less robust (fig. S5C).

Despite these limitations, the congruence of these changes in the seasonality around the turn of the millennium with the decadal variations of the Southern Ocean carbon sink (*18*–*20*) merits further discussion. For the period 2000–2018, when significant and robust increases in seasonal differences in air-sea flux are estimated from the six datasets (*24*, *28*–*32*) (33 [27, 39] Tg C decade^{-1}), significant increasing trends in the annual ocean carbon uptake are found together in all datasets (200 [141, 244] Tg C decade^{-1}) (fig. S6). Similarly, significant trends in ocean carbon sink are not estimated before 2000 (i.e., 1986–1999; 1.8 [−94, 85] Tg C decade^{-1}) when the trend of seasonal difference in the air-sea flux is absent (5.9 [−14, 29] Tg C decade^{-1}). Before we discuss the reasons underlying this connection between variations in seasonality and annual fluxes, we first need to put the qualitative conclusions about the attribution of the observed changes in AMP on a quantitative basis.

Attributions of changes in the seasonal amplitude of atmospheric CO_2

To this end, we performed GEOS-Chem model simulations for 2000–2016 (see Materials and Methods for details) using gridded estimates of the net terrestrial CO_2 flux (CLM4.5) (*33*), of different air-sea CO_2 fluxes [CAMS (*24*), Jena-MLS (*29*), and Ocean-SODA-ETHZ (*32*)], and of $FFCO_2$ emissions [ODIAC (*34*) and PKU-CO_2 (*35*)]. The impacts of changes in the three components are evaluated on the basis of differences between our base simulation, $ALL_{transient}$, wherein all variables are transient, and the factorial simulations VEG_{2000}, OCN_{2000}, and FF_{2000}, wherein each CO_2 flux component is repeatedly prescribed during the simulation period using the fluxes for the year 2000. The effects of the other factors (i.e., atmospheric transport and biomass burning) are evaluated from the ALL_{2000} simulation, wherein the CO_2 fluxes of the three components are repeatedly prescribed at their 2000 values. We limit our simulation to the period after 2000 because of the better consistency between the datasets in estimating the changes in air-sea CO_2 flux seasonality.

Annual trends in the simulated AMP from the base simulation $ALL_{transient}$ exhibit clear latitudinal gradients in the NH, a pattern consistent with observations and inverse modeling estimates for 2000–2018 (Fig. 3A). Stronger positive trends in AMP (1.1 [1.0, 1.1] ppm decade^{-1}) are detected in the Arctic (around 70°N) than in the tropics (0.24 [0.20, 0.27] ppm decade^{-1}). In addition, a significant positive trend in AMP (0.16 [0.09, 0.22] ppm decade^{-1}) is found around 60°S, of similar magnitude to the observed trend. Furthermore, the model generally captures the timing of the seasonal maximum and minimum in atmospheric CO_2 (i.e., phase) with an average lead or lag time of approximately 1 month (fig. S7). At the station level, the simulated seasonal variations are in good agreement with the observed seasonal variations (e.g., r = 0.96, 0.96, 0.92, and 0.86 at BRW, MLO, PSA, and SPO stations, respectively; fig. S8). In the tropics and the southern high latitudes, our model simulates the mean AMP within ±10% of the observed values (fig. S8, B to D), but it underestimates AMP in the Arctic (e.g., capturing 76% of the observed mean value at BRW; fig. S8A) because of a negative bias in the terrestrial flux of the Arctic biomes in CLM4.5-CN (*36*). Although this bias might lead to an underestimation of the contribution of terrestrial ecosystems to the AMP trends at the northern high latitudes, our factorial simulations can be considered appropriate for evaluating the influence of surface CO_2 fluxes on changes in AMP, especially in the SH, the main area of interest.

The factorial simulations show that terrestrial ecosystems and oceans are the dominant factors driving changes in AMP at high latitudes in the NH and SH, respectively. The increasing seasonality of terrestrial fluxes dominates the increase of AMP north of 45°N, accounting for 82% [81, 83%] of the observed AMP trend over this region for 2000–2018 (1.01 [1.00, 1.02] ppm decade^{-1}) (Fig. 3, B and C). The increasing seasonality of the air-sea fluxes in the northern North Atlantic Ocean and Greenland Sea partly reinforces the increase in the northern AMP by 0.05 [0.01, 0.07] ppm decade^{-1} (Fig. 3, B and D). In contrast, the increasing seasonality of air-sea fluxes explains most of the enhancement of AMP south of 45°S, accounting for 67% [50, 83%] of the observed AMP trend from 2000 to 2018 (0.14 [0.10, 0.17] ppm decade^{-1}). By conducting an additional sensitivity experiment where the Southern Ocean (south of 40°S) follows a perpetual seasonal cycle of the year 2000, while the rest of the ocean is allowed to vary (analogous to the OCN_{2000} simulation), we find that the changes in this region alone cause a 115% increase in AMP south of 45°S (fig. S9). This accounts for most of the observed changes, confirming that the increase in AMP south of 45°S after the turn of the millennium is primarily due to the seasonal amplification of the air-sea CO_2 flux in the Southern Ocean.

Besides the dominating contribution of the changing seasonality of the land and ocean fluxes to observed changes in AMP, we need to pay attention also to the other factors, primarily the effect of the

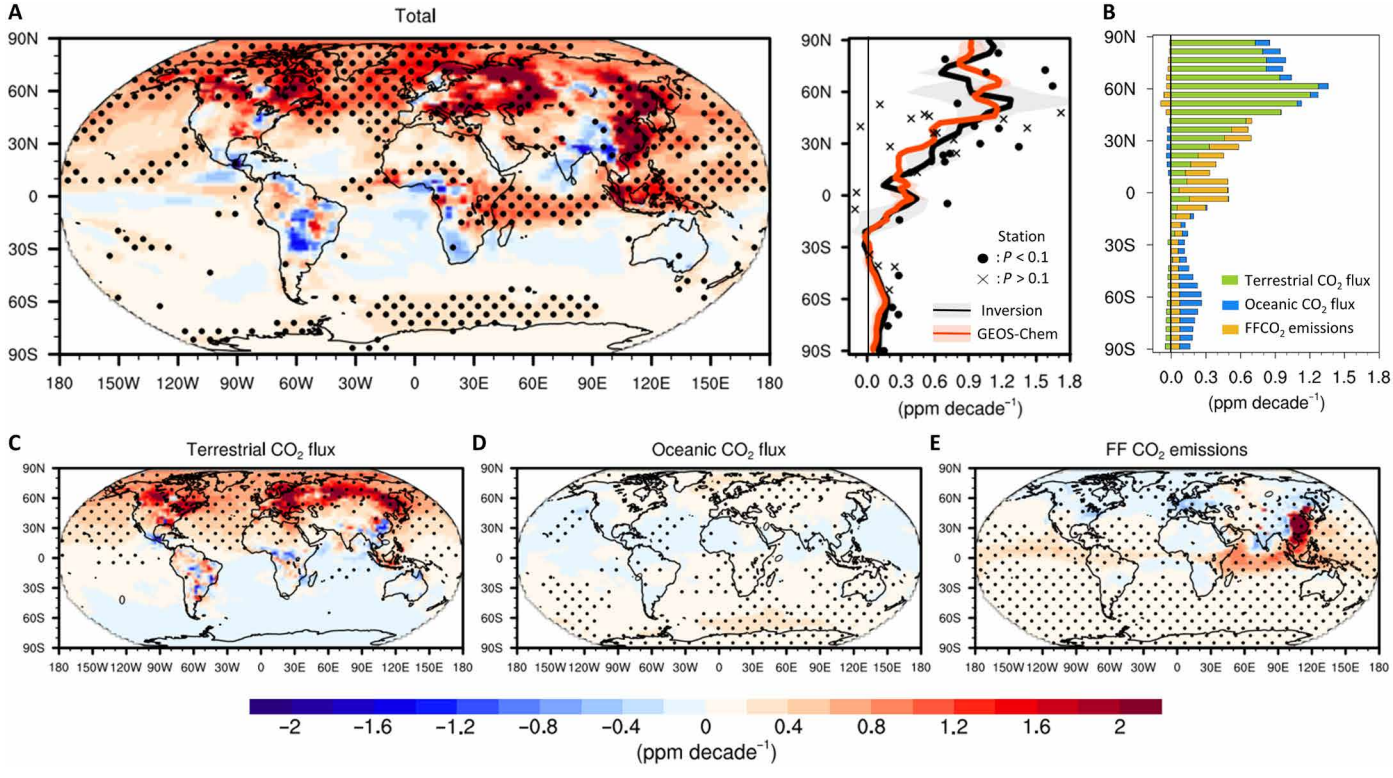

Fig. 3. Changes in seasonal amplitude of atmospheric CO_2 (AMP) and drivers. (**A** and **C** to **E**) Simulated annual trends in AMP from 2000 to 2016 ($ALL_{transient}$; A) and contributions of terrestrial CO_2 exchange ($ALL_{transient}$ minus BIO_{2000}; C), ocean CO_2 exchange ($ALL_{transient}$ minus OCN_{2000}; D), and fossil fuel CO_2 ($FFCO_2$) emissions ($ALL_{transient}$ minus FF_{2000}; E) to this trend estimated from factorial simulations with a global atmospheric transport model (see Materials and Methods). The stippled areas represent statistically significant annual trends ($P < 0.05$, two-tailed Student's t test). In (A), the right-hand panel shows zonally averaged latitudinal distributions of the mean (thick orange line) with 95% confidence intervals based on 1000 bootstrap samples (shaded area) of simulations. The scatters and black line indicate AMP trends for the observations at surface stations and the estimation from two inverse modeling (CAMS and Jena) with its range (shaded area) for 2000–2018. Among nonshown five outliers, a significant value (2.47 ppm decade^{-1}; $P < 0.1$ at LEF) is included in the analysis, but nonsignificant values ($P > 0.1$) with <−0.4 ppm decade^{-1} (CBA, KEY, and EIC) or >3 ppm decade^{-1} (FSD) are excluded. (**B**) Contributions to zonally averaged trends of simulated AMP per 5° latitudes.

strong increase in the fossil fuel emissions ($FFCO_2$), and the resulting changes in the atmospheric CO_2 gradients. It turns out that the increasing $FFCO_2$ emissions have contributed to the increase of AMP in the tropics and even the SH, but its magnitude drops to 0.08 and 0.07 ppm decade^{-1} north of 45°N and south of 45°S, respectively (Fig. 3, B and E). Changes in atmospheric transport and biomass burning also tend to reduce AMP over the tropics by 0.08 ppm decade^{-1} (fig. S10). However, because their effects are spatially heterogeneous with opposite signs, their zonally averaged AMP, especially in the SH, is very small. These findings support the conclusions that the increases in AMP observed at high latitudes is mostly induced by alterations in natural carbon fluxes, from the land in the NH and from the ocean in the SH.

Processes driving the changes in the seasonality of air-sea CO_2 flux in the Southern Ocean

To gain insights into the oceanic processes responsible for the changes in seasonality of air-sea fluxes in the Southern Ocean, we explore the drivers of the trends in the seasonal difference of PCO_2, the dominant variable modulating the air-sea CO_2 flux (*37*, *38*). Seasonal variations in PCO_2 are controlled by sea surface temperature (SST) and by nonthermal factors such as dissolved inorganic carbon (DIC), alkalinity (Alk), and freshwater (FW) fluxes (diagnosed through changes in salinity). In the Southern Ocean, seasonal minima and maxima of PCO_2 typically occur in winter and summer, respectively, and are driven primarily by the seasonal changes in DIC. These are a result of biological uptake of DIC in summer and deep ocean mixing reconstituting most of the DIC (*39*–*41*). Among the PCO_2 datasets, the Ocean-SODA-ETHZ product provides PCO_2 as well as all other carbonate system variables (*32*), permitting us to investigate the causes of the opposing trends of surface ocean PCO_2 seasonality before and after 2000.

Using a linear Taylor series expansion of the changes in seasonal PCO_2 differences in terms of its four components [i.e., sDIC (salinity-normalized DIC), sAlk (salinity-normalized Alk), FW, and SST] (see Materials and Methods for details), we explore the following three potential mechanisms to explain the enhanced seasonality of PCO_2: (i) increasing PCO_2 sensitivity to seasonal changes in each component (e.g., by reducing the ocean's buffering capacity); (ii) increasing seasonal variability of PCO_2 in proportion to annual PCO_2, assuming a constant PCO_2 sensitivity, i.e., a "mass effect"; and (iii) increasing seasonal differences in the drivers of the seasonality, i.e., changes in sDIC, sAlk, FW, and SST due to biogeophysical processes, such as biological uptake, mixing, warming (cooling), and ice melt. The first two mechanisms are intimately tied to ocean acidification stemming from the ocean's absorption of anthropogenic CO_2 (*42*). The third mechanism is primarily associated with variability driven by natural processes. We overall follow the decomposition analysis presented by Landschützer *et al.* (*22*); however, the PCO_2 sensitivity to DIC and Alk is exactly calculated considering a full carbonate system model rather than approximations.

The linear decomposition analysis reproduces the original trends of the seasonal differences in PCO_2 relatively accurately for the period 2000–2018 (capturing 98% of the original trends) (Fig. 4A and Table 1). This fraction is only 65% for the period 1986–1999 because the signal is much weaker so that neglected nonlinear terms matter more. Recognizing this limitation for the period before 2000, this linear decomposition allows us to assess the contribution of each of the three mechanisms. Our analysis reveals that the increase in surface ocean PCO_2, i.e., the mass effect, is the most important driver of the changes in seasonality for the period 2000–2018, thus confirming the results of (*22*). The mass effect enhances the seasonal contribution of sDIC (1.85 [1.72, 1.97] µatm decade^{-1}) more than it affects the contribution of SST (1.38 [1.28, 1.47] µatm decade^{-1}) (Fig. 4B). This leads to an amplification of the seasonal cycle in PCO_2 in the Southern Ocean, as it is primarily controlled by the seasonality of sDIC. The reduced buffer capacity, i.e., the increase in the PCO_2 sensitivity to sDIC, is the second most important factor contributing to the increase in the seasonal difference of PCO_2 (0.65 [0.57, 0.73] µatm decade^{-1}). The seasonal changes in the drivers also act to augment the anthropogenic seasonal amplification of PCO_2 (1.01 [0.54, 1.47] µatm decade^{-1}).

Different results are found for the period 1986–1999. While the increases in PCO_2 (0.57 [0.50, 0.65] µatm decade^{-1}) and the PCO_2 sensitivity to sDIC (0.80 [0.66, 0.94] µatm decade^{-1}) had tended to increase the seasonal difference of PCO_2 (Fig. 4B), other factors tended to reduce the seasonal difference. Particularly relevant is the decreasing trend induced by the decreasing seasonal differences in

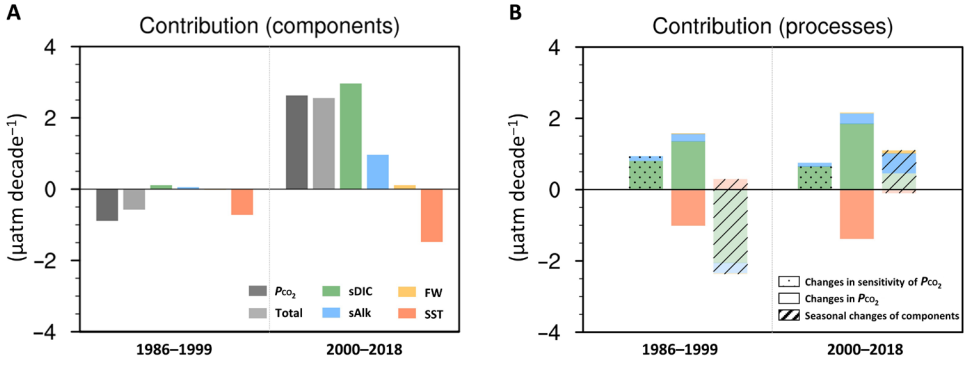

Fig. 4. Causes of changes in seasonal differences in Pco_2 in the Southern Ocean. (**A**) Area-weighted trends of seasonal differences in Pco_2 derived from the OceanSODA-ETHZ dataset for 1986–1999 and 2000–2018 and contributions of sDIC, sAlk, FW, and SST to the trends. The estimated trend is shown in dark gray bars (denoted as Pco_2), whereas the sum of the decomposed contributions is shown in light gray bars (denoted as Total). (**B**) Contributions of changes in the sensitivity of Pco_2, annual Pco_2, and seasonal differences for each component [shown in the colors indicated in (A)] described in the first, second, and third terms on the right-hand side of equations (Eqs. 8 to 11) in Materials and Methods, respectively. Dark- and light-colored bars in (B) represent significant trends ($P < 0.05$, two-tailed Student's t test) and nonsignificant trends ($P > 0.05$), respectively.

Table 1. Area weighted trends of seasonal difference of P_{CO_2} in the Southern Ocean and its drivers. Linear regression coefficients (Co-eff) and 95% confidence intervals ($CI_{95\%}$) of the seasonal difference (winter minus summer) in P_{CO_2} derived from the OceanSODA-ETHZ dataset for 1986–1999 and 2000–2018 and contributions of salinity-normalized dissolved inorganic carbon (sDIC), salinity-normalized alkalinity (sAlk), freshwater (FW), and sea surface temperature (SST) to the trends. Units of Co-eff and $CI_{95\%}$ are µatm decade^{-1}.

		Periods			
		1986–1999		2000–2018	
		Co-eff	$CI_{95\%}$	Co-eff	$CI_{95\%}$
Original P_{CO_2}		−0.88 ($P < 0.05$)	−1.72:−0.05	2.61 ($P < 0.05$)	2.11:3.12
Factor	Mechanism				
sDIC	P_{CO_2} sensitivity	0.80 ($P < 0.05$)	0.66:0.94	0.65 ($P < 0.05$)	0.57:0.73
	P_{CO_2}	1.35 ($P < 0.05$)	1.17:1.54	1.85 ($P < 0.05$)	1.72:1.97
	Seasonal change	−2.05 ($P = 0.13$)	−4.78:0.68	0.46 ($P = 0.35$)	−0.55:1.47
sAlk	P_{CO_2} sensitivity	0.13 ($P < 0.05$)	0.11:0.15	0.11 ($P < 0.05$)	0.09:0.12
	P_{CO_2}	0.21 ($P < 0.05$)	0.18:0.24	0.29 ($P < 0.05$)	0.27:0.31
	Seasonal change	−0.29 ($P = 0.75$)	−2.25:1.67	0.56 ($P < 0.05$)	0.17:0.95
FW	P_{CO_2} sensitivity	0.00 ($P < 0.05$)	0.00:0.00	0.00 ($P < 0.05$)	0.00:0.00
	P_{CO_2}	0.02 ($P < 0.05$)	0.01:0.02	0.02 ($P < 0.05$)	0.02:0.03
	Seasonal change	−0.02 ($P = 0.89$)	−0.30:0.27	0.08 ($P < 0.05$)	0.03:0.13
SST	P_{CO_2} sensitivity	–	–	–	–
	P_{CO_2}	−1.01 ($P < 0.05$)	−1.14:−0.87	−1.38 ($P < 0.05$)	−1.47:−1.28
	Seasonal change	0.29 ($P = 0.49$)	−0.60:1.17	−0.09 ($P = 0.80$)	−0.84:0.66
Sum		−0.57	−1.41:0.26	2.55	2.13:2.96

sDIC, which compensate for the anthropogenic seasonal amplification of P_{CO_2} (2.05 [−0.68, 4.78] µatm decade^{-1}). The results thus suggest that while the anthropogenic-driven changes in CO_2, acting through the mass effect and ocean acidification, drive up the seasonal cycle of P_{CO_2} in the Southern Ocean across the four decades, natural DIC-driven changes overcompensate these trends before 2000. This leads to the negative trend in the seasonal difference in P_{CO_2} before 2000 and a positive trend after 2000.

This finding permits us to link the changes in the P_{CO_2} difference to the changes in the magnitude of the Southern Ocean carbon sink. The strong reduction in this sink during the 1990s has been attributed primarily to an increase in the upwelling of natural carbon from below in response to an intensification and southward displacement of the westerly winds (*17*, *20*, *43*) associated with a strong positive trend of the Southern Annular Mode (*44*). This increased upwelling then led to anomalously strong outgassing of natural CO_2 to the atmosphere, overwhelming the trend for an increased uptake of anthropogenic CO_2 (*43*). The diagnosed reduced seasonality of sDIC that drives the reduced seasonality during the period before 2000 is likely connected to the increase in upwelling as well. Although we lack information on the seasonality of upwelling and vertical transport/mixing of DIC in general, it is feasible that this enhanced vertical transport/mixing occurred year-round. Given the strong seasonality of the surface mixed layer, this would imply that this enhanced vertical transport reduces the impact of the biological sDIC drawdown in summer more than it increases the impact in winter. This may lead to much higher sDIC in summer, and marginally higher sDIC in winter, or overall to a reduced seasonal difference in sDIC. This mechanism would explain the observed congruent changes in the seasonal difference and the annual carbon sink on decadal time scales.

Given this interaction between natural and anthropogenic CO_2 components driving changes in the seasonal difference of P_{CO_2}, it is difficult to predict whether the current anthropogenic-driven seasonal amplification in air-sea CO_2 flux will continue. We thus resort to simulation results from the Community Earth System Model 2 large ensemble (CESM2-LE) (*45*). CESM2-LE projects under the high emission scenario (SSP370) that the seasonal amplitude of air-sea CO_2 flux will rapidly increase in the Southern Ocean for the 21st century because of growing impacts of the invasion of anthropogenic

CO_2 into the oceans (fig. S11A), in line with other modeling studies (*46*–*48*). Time of emergence analyses (see Materials and Methods for details) reveals that the anthropogenic forcing becomes statistically distinguishable from the natural variability at the 95% confidence level after 2002 (fig. S11B). The results suggest that the observed significant increasing trend of seasonal amplitude of air-sea CO_2 flux and atmospheric CO_2 after around 2000 is an inevitable consequence of rising atmospheric CO_2 and the increases will continue in the future.

DISCUSSION

Significant increases in AMP are observed not only at northern high latitudes but also at southern high latitudes for 2000–2018. In contrast, most trends in AMP before the year 2000 are either statistically insignificant or even negative, and especially at southern high latitudes. By using models and surface ocean PCO_2-based reconstructions, we demonstrated that the decadal variations in the AMP at southern high latitudes are mostly caused by decadal changes in the seasonal air-sea CO_2 exchange in the Southern Ocean. During the period before the turn of the millennium, the reduced seasonality of the PCO_2 caused a decrease in the AMP, while the opposite situation occurred after 2000. A PCO_2 decomposition analysis suggests that before 2000, a substantial decrease in the seasonal difference of sDIC caused the reduction in the PCO_2 seasonality. This was likely caused by the enhanced upwelling of natural CO_2 that prevailed during the 1990s and which is the key driver for the weakening carbon sink in the Southern Ocean during this period (*20*). In contrast, for the period after 2000, the PCO_2 decomposition analysis reveals that increasing anthropogenic CO_2 uptake in the oceans plays a first-order role in the seasonal amplification of air-sea CO_2 fluxes, in the same way that the CO_2 fertilization effect in terrestrial ecosystems is thought to be a key driver of increasing AMP in the NH (*5*–*10*). Multiple lines of evidence presented in this study indicate that anthropogenic disruption of the carbon cycle in both oceans and terrestrial ecosystems has been sufficiently intensified over the past several decades to now be detectable in the atmosphere.

Although five different observation-based PCO_2 datasets consistently show amplification of the seasonal difference in PCO_2 in the Southern Ocean for the past two decades and a lack of a trend before 2000, it should be noted that the differences between the different products are considerable, particularly for the first period. This is not surprising since observations tend to be very sparse and generally have a summer bias (*49*, *50*). This hampers the accurate quantification of the effects of natural processes (*51*). The seasonal sampling biases then lead to uncertainty in diagnoses of changes in PCO_2 seasonality and subsequently model simulations (*52*–*54*), causing considerable uncertainties in future projections of the ocean carbon sink (*54*). Measurements from recently initiated year-round floats (*55*–*57*), providing information on essential biophysical and chemical properties of the world's oceans over the entire season, will help to reduce this uncertainty by filling the gaps in the ship-based observing system. Moreover, continuous monitoring of atmospheric CO_2 could provide additional information concerning changes in ocean processes and for use in assessment of model performance (*16*).

Our results focused on the Southern Ocean show that while there is substantial decadal modulation of the air-sea CO_2 flux seasonality, it is bound to be strengthened as long as atmospheric CO_2 keeps rising and the ocean keeps taking up anthropogenic CO_2 from the atmosphere in response. This is because this uptake of anthropogenic CO_2 increases oceanic PCO_2 and modifies the CO_2 chemistry, both of which increase the seasonality of the surface ocean PCO_2 and hence the seasonality of the air-sea CO_2 fluxes. Concomitant with this seasonal amplification in PCO_2 is the seasonal amplification of *p*H (*58*, *59*) that exposes marine species, which are sensitive to ocean acidification, to harmful conditions much earlier than predicted from the long-term trend (*58*).

By recording these changes in the seasonality of the carbon cycle in the Southern Ocean, measurements of atmospheric CO_2 may thus provide a window into the study of the unfolding dynamics of the Southern Ocean carbon cycle. It is particularly intriguing that the changes in the seasonality tend to go hand in hand with the changes in the annual strength of the Southern Ocean carbon sink. Given the extraordinary role of this region in the uptake of CO_2 from the atmosphere, monitoring this sink is essential. The recent work of Long *et al.* (*16*) demonstrated already the great value of atmospheric CO_2 observations for constraining the Southern Ocean carbon sink. Our work adds to this growing evidence by pointing out the fact that one can now tease apart changes in the seasonality of atmospheric CO_2, i.e., its AMP, permitting us to draw conclusions about changes in the seasonality of the Southern Ocean carbon sink, with important implications also for marine life. Therefore, the response of the ocean system to increasing anthropogenic perturbations should be continuously monitored on the basis of a comprehensive understanding of ocean chemical and biophysical processes that determine the changes in ocean sink efficiency.

MATERIALS AND METHODS

Atmospheric CO_2 measurements

Weekly (or biweekly) flask measurements and continuous measurement datasets for atmospheric CO_2 concentrations worldwide are provided by the World Data Center for Greenhouse Gases (*1*, *60*, *61*). Long-term measurement datasets at 16 stations (white box in table S1) for 1980–2018 are used to compare changes in AMP before and after 2000. Additional datasets from 33 stations covering the period 2000–2018 are also used (gray box in table S1) to support our findings, which are derived from long-term datasets from 16 stations. The longest dataset or flask measurement dataset is preferred when both types of CO_2 measurements are performed simultaneously.

To extract the seasonal cycle of atmospheric CO_2 for each station, we use a standard package from the National Oceanic and Atmospheric Administration Earth System Research Laboratories (NOAA-ESRL) (CCGCRV; https://gml.noaa.gov/aftp/user/thoning/ccgcrv/) (*62*). In the data analysis software, weekly or hourly observation data are fitted with a quadratic polynomial and four harmonics function, as shown below

$$f(t) = a_0 + a_1 t + a_2 t^2 + a_3 \sin(2\pi t) + a_4 \cos(2\pi t) + a_5 \sin(4\pi t) + a_6 \cos(4\pi t) \quad (1)$$

Low-pass filters with 80 and 667 cutoff days are then applied to the residuals of the functional fit to capture the short-term and interannual variations not derived by Eq. 1. Seasonal cycle of atmospheric CO_2 is obtained by combining harmonic terms of the function and residuals smoothed by the short-term filter. The AMP is calculated from the difference between the maximum and minimum of the CO_2 seasonal cycle each year.

Breakpoint analysis

A segmented linear regression model is used to test whether there is a significant shift in the temporal trends in the AMP and to determine the timing of the significant change in the trends (i.e., a breakpoint). The model calculates the sum of squares of the differences between the original values (X) and linearly fitted values in each segment (Y_1 and Y_2), and identifies the breakpoint that minimizes the sum of squared residuals as follows

$$\begin{cases} Y_1 = \alpha_1 X + \epsilon_1 \ (x \leq \text{Breakpoint}) \\ Y_2 = \alpha_2 X + \epsilon_2 \ (x > \text{Breakpoint}) \end{cases} \quad (2)$$

Here, α and ϵ represent linear regression coefficients and regression constants in each segment, respectively. Because our study focuses on long-term changes in AMP, an 11-year running averaged AMP is applied to the segmented regression model. The significance of the difference between the slopes before and after the breakpoint is then tested using a t test (*63*) based on the original AMP values.

Atmospheric inversion datasets

Inverse modeling estimates the optimized surface CO_2 flux and three-dimensional atmospheric CO_2 fields from prior surface CO_2 flux datasets using atmospheric CO_2 measurements and a transport model. The CAMS inversion dataset (v18r3) (*24*) is produced using continuous or flask measurements at 129 sites across the planet and the Laboratoire de Météorologie Dynamique global transport model for 1979–2018. The Jena inversion dataset (v4.3) (*25*) is produced using continuous or flask measurements at 89 sites around the world and Transport Model 3 for 1957–2018. Atmospheric CO_2 concentrations at the surface in two different inversion datasets are used to identify the latitudinal features of changes in AMP during 1980–2018. The air-sea CO_2 flux in CAMS dataset is used to examine the changes in seasonality of air-sea CO_2 exchange for the study period, together with Pco_2-based data products.

Pco_2-based products

The air-sea CO_2 flux (Fco_2) is calculated from the following equation

$$Fco_2 = K_W \cdot S_{CO_2} \cdot (1 - [\text{ice}]) \cdot (Pco_2 - Pco_2^{atm}) \quad (3)$$

Here, K_w, S_{CO2}, Pco_2, Pco_2^{atm}, and [ice] represent the gas transfer velocity for CO_2, CO_2 solubility, oceanic and atmospheric CO_2 partial pressure, and ice fraction, respectively. To examine the changes in the seasonality of air-sea CO_2 flux for 1980–2018 and the causes of the changes, five different globally mapped Fco_2 and Pco_2 datasets based on global Pco_2 measurements (Surface Ocean CO_2 Atlas) (*49*) are used: Jena-MLS (oc_v2020), OceanSODA-ETHZ, MPI-SOMFFN, CSIR-ML6, and CMEMS-FFNN.

Jena-MLS estimates the air-sea CO_2 flux based on an extended inversion framework considering atmospheric transport along with internal processes in the oceanic mixed layer (*29*). The other datasets apply nonlinear regression techniques to derive the relationship between Pco_2 and driving variables, including SST, sea surface salinity, mixed layer depth, and chlorophyll a, to map surface ocean Pco_2 worldwide. OceanSODA-ETHZ adopts a 16-member ensemble approach, where each member clusters the global ocean into 21 regions based on climatological ocean states with different initial conditions. Half of the ensemble members apply feed-forward neural networks (FFNs) to each cluster, and the other half use gradient boosted decision trees (*32*). The average of the 16 ensemble estimates is used in this study. Because the dataset does not provide air-sea CO_2 fluxes, we estimate them using K_w, S_{CO2}, [ice], and Pco_2^{atm} in the SeaFlux datasets (*64*). MPI-SOMFFN clusters the global ocean into 16 areas using a self-organizing map (SOM) and applies FFN method (*30*). CSIR-ML6 provides six ensemble members of Pco_2 estimated by applying three different mapping methods to two clustering instances, where the mapping methods are support vector regression, FFN, and gradient-boosted regression trees (*31*). The ensemble average of six estimates is used in this study. The CMEMS-FFNN applies 12 FFNN models to map Pco_2 for every month of the year (*28*).

To identify the changes in seasonal differences in air-sea CO_2 fluxes and Pco_2, monthly variables are fitted with a quadratic polynomial and four harmonics function (Eq. *2*) for all study years (*5*, *22*). Seasonal variations for individual years are derived from harmonic terms in the fitted function to data for a specific year and the year before and after. Seasonal differences of each variable in the NH are computed using the differences in values for winter (December to February) and summer (June to August), and vice versa in the SH. The same method is applied to calculate the seasonal difference in terrestrial CO_2 flux used for comparison with that of air-sea CO_2 flux.

GEOS-Chem model simulations

The GEOS-Chem model is an atmospheric chemical transport model (*65*) that simulates atmospheric CO_2 from the hourly Modern Era Retrospective analysis for Research and Applications (version 2) reanalysis meteorological datasets (*66*) and surface CO_2 flux datasets. This model includes terrestrial and ocean CO_2 fluxes and emissions from FF combustion, biomass burning, shipping, and aviation. The monthly averaged net ecosystem production simulated from the Community Land Model (version 4.5) with a carbon-nitrogen module (*33*, *67*) is used to estimate the terrestrial CO_2 flux. Of the six different datasets included in our analysis, air-sea CO_2 fluxes from the CAMS, Jena-MLS, and OceanSODA-ETHZ datasets are used in the model simulations. Estimates of $FFCO_2$ emissions are obtained from the open-source data inventory for anthropogenic CO_2 (ODIAC; doi:10.17595/20170411.001) (*34*) and the Peking University CO_2 inventory (PKU-CO_2; http://inventory.pku.edu.cn/download/download.html) (*35*); estimates of emissions from the biomass burning are obtained from the Global Fire Emissions Database (*68*).

To evaluate the influence of terrestrial and ocean CO_2 fluxes and $FFCO_2$ emissions on changes in AMP, four sets of model simulations are conducted. Following 10 years of spin-up, a set of model simulations is conducted with 2° × 2.5° spatial resolution for the period 2000–2016 (2014 for PKU-CO_2), as the simulated terrestrial CO_2 flux covers the period until 2016 due to the lack of a climate forcing dataset for 2017–2018. Transient meteorological variables and surface CO_2 fluxes are used in $ALL_{transient}$ (i.e., control simulation). In BIO_{2000}, OCN_{2000}, and FF_{2000}, the 2000 values of terrestrial CO_2 flux, air-sea CO_2 fluxes, and $FFCO_2$ emissions are repeatedly prescribed over the globe during the simulation period, respectively, while the other conditions are the same as those of the control simulation. We estimate the influence of each factor on changes in AMP based on the differences between $ALL_{transient}$ and BIO_{2000}, OCN_{2000}, and FF_{2000}. We repeat the set of model simulations by

switching the air-sea CO_2 flux datasets (CAMS, Jena-MLS, and OceanSODA-ETHZ) and $FFCO_2$ emission datasets (ODIAC and PKU-CO_2) to provide the estimated ranges of influence for each factor. Then, we apply the same smoothing and filtering method with observations to the simulated monthly mean atmospheric CO_2 concentrations at the surface to calculate AMP.

Additional simulation sets are also conducted. First, we prescribe CO_2 fluxes of the three components (i.e., terrestrial and ocean CO_2 fluxes and $FFCO_2$ emissions) repeatedly in their 2000 values globally for 2000–2016 (ALL_{2000}) to evaluate the potential influences of atmospheric circulation and biomass burning on the observed changes in AMP. In addition, regional influences of changes in air-sea CO_2 flux in the Southern Ocean are evaluated from the difference between $ALL_{transient}$ and OCN_SO_{2000} simulations, in which monthly air-sea CO_2 fluxes are repeatedly prescribed at their 2000 values in the Southern Ocean during 2000–2016. The ODIAC $FFCO_2$ emission and OceanSODA-ETHZ ocean CO_2 flux datasets are used for the additional simulations.

Driver decomposition of the trends of seasonal differences in P_{CO_2}

To understand the causes of seasonal changes in P_{CO_2}, we calculate a first-order Taylor series expansion of P_{CO_2} in terms of SST, sDIC, sAlk, and FW using the OceanSODA-ETHZ dataset, which provides all carbonate system parameters, and the Operational Sea Surface Temperature and Sea Ice Analysis (*69*) dataset. Salinity is from the EN4.2.1 optimally interpolated analysis (*70*). Temporal P_{CO_2} variations can be expressed following Landschützer *et al.* (*22*)

$$\mathrm{d}P_{CO_2} = \frac{\partial P_{CO_2}}{\partial \mathrm{SST}} \cdot \mathrm{dSST} + \frac{\partial P_{CO_2}}{\partial \mathrm{DIC}} \cdot \mathrm{dsDIC} + \frac{\partial P_{CO_2}}{\partial \mathrm{Alk}} \cdot \mathrm{dsAlk} + \frac{\partial P_{CO_2}}{\partial \mathrm{FW}} \cdot \mathrm{dFW} \quad (4)$$

where $\mathrm{sDIC} = \frac{S_{ref}}{S} \cdot \mathrm{DIC}$ and $\mathrm{sAlk} = \frac{S_{ref}}{S} \cdot \mathrm{Alk}$

where we use the local long-term mean salinity (S_{ref}) to normalize DIC and Alk, i.e., to remove the FW flux effects on seasonal variations. The sensitivities of P_{CO_2} to changes in each component are defined as follows

$$\gamma_T = \frac{1}{P_{CO_2}} \frac{\partial P_{CO_2}}{\partial \mathrm{SST}}, \gamma_{\mathrm{DIC}} = \frac{\mathrm{DIC}}{P_{CO_2}} \frac{\partial P_{CO_2}}{\partial \mathrm{DIC}}, \gamma_{\mathrm{Alk}} = \frac{\mathrm{Alk}}{P_{CO_2}} \frac{\partial P_{CO_2}}{\partial \mathrm{Alk}}, \text{ and } \gamma_{\mathrm{FW}} = \frac{\mathrm{FW}}{P_{CO_2}} \frac{\partial P_{CO_2}}{\partial \mathrm{FW}} \quad (5)$$

The equation used to calculate variations in P_{CO_2} can then be rewritten in terms of seasonal differences (i.e., Δ^{ss})

$$\Delta^{ss} P_{CO_2} = \gamma_T \cdot P_{CO_2} \cdot \Delta^{ss}\mathrm{SST} + \gamma_{\mathrm{DIC}} \cdot \frac{P_{CO_2}}{\mathrm{DIC}} \cdot \Delta^{ss}\mathrm{sDIC} + \gamma_{\mathrm{Alk}} \cdot \frac{P_{CO_2}}{\mathrm{Alk}} \cdot \Delta^{ss}\mathrm{sAlk} + \gamma_{\mathrm{FW}} \cdot \frac{P_{CO_2}}{\mathrm{FW}} \cdot \Delta^{ss}\mathrm{FW} \quad (6)$$

The P_{CO_2} sensitivity to temperature (γ_T) is approximated by $0.0423°C^{-1}$ (*27*). The P_{CO_2} sensitivities with respect to DIC (γ_{DIC}) and Alk (γ_{Alk}) are calculated with the PyCO2SYS software (*71*), using a gradient approach. This substantially improves the accuracy compared to the use of the approximations from Sarmiento and Gruber (*27*) as done by the previous study (*22*). Last, the P_{CO_2} sensitivity to FW (γ_{FW}) is derived from the sum of the P_{CO_2} sensitivity to DIC, Alk, and salinity (γ_S is approximated by 1) (*27*).

Last, we determine the time derivative of the equation and calculate the contributions of three major processes to the annual trends of seasonal differences in P_{CO_2} for each of the four components by permitting temporal variations in only one of the terms while maintaining the others at their long-term mean

$$\frac{d\Delta^{ss}P_{CO_2}}{dt} = \frac{d\Delta^{ss}P_{CO_2}^{\mathrm{SST}}}{dt} + \frac{d\Delta^{ss}P_{CO_2}^{\mathrm{sDIC}}}{dt} + \frac{d\Delta^{ss}P_{CO_2}^{\mathrm{sAlk}}}{dt} + \frac{d\Delta^{ss}P_{CO_2}^{\mathrm{FW}}}{dt} \quad (7)$$

$$\frac{d\Delta^{ss}P_{CO_2}^{\mathrm{SST}}}{dt} = \frac{d\gamma_T}{dt} \cdot \overline{P_{CO_2}} \cdot \overline{\Delta^{ss}\mathrm{SST}} + \overline{\gamma_T} \cdot \frac{dP_{CO_2}}{dt} \cdot \overline{\Delta^{ss}\mathrm{SST}} + \overline{\gamma_T} \cdot \overline{P_{CO_2}} \cdot \frac{d\Delta^{ss}\mathrm{SST}}{dt} \quad (8)$$

$$\frac{d\Delta^{ss}P_{CO_2}^{\mathrm{sDIC}}}{dt} = \frac{d\gamma_{\mathrm{DIC}}}{dt} \cdot \frac{\overline{P_{CO_2}}}{\overline{\mathrm{DIC}}} \cdot \overline{\Delta^{ss}\gamma} + \overline{\gamma_{\mathrm{DIC}}} \cdot \frac{d}{dt}\left(\frac{P_{CO_2}}{\mathrm{DIC}}\right) \cdot \overline{\Delta^{ss}\mathrm{sDIC}} + \overline{\gamma_{\mathrm{DIC}}} \cdot \frac{\overline{P_{CO_2}}}{\overline{\mathrm{DIC}}} \cdot \frac{d\Delta^{ss}\mathrm{sDIC}}{dt} \quad (9)$$

$$\frac{d\Delta^{ss}P_{CO_2}^{\mathrm{sAlk}}}{dt} = \frac{d\gamma_{\mathrm{Alk}}}{dt} \cdot \frac{\overline{P_{CO_2}}}{\overline{\mathrm{Alk}}} \cdot \overline{\Delta^{ss}\mathrm{sAlk}} + \overline{\gamma_{\mathrm{Alk}}} \cdot \frac{d}{dt}\left(\frac{P_{CO_2}}{\mathrm{Alk}}\right) \cdot \overline{\Delta^{ss}\mathrm{sAlk}} + \overline{\gamma_{\mathrm{Alk}}} \cdot \frac{\overline{P_{CO_2}}}{\overline{\mathrm{Alk}}} \cdot \frac{d\Delta^{ss}\mathrm{sAlk}}{dt} \quad (10)$$

$$\frac{d\Delta^{ss}P_{CO_2}^{\mathrm{FW}}}{dt} = \frac{d\gamma_{\mathrm{FW}}}{dt} \cdot \frac{\overline{P_{CO_2}}}{\overline{\mathrm{FW}}} \cdot \overline{\Delta^{ss}\mathrm{FW}} + \overline{\gamma_{\mathrm{FW}}} \cdot \frac{dP_{CO_2}}{dt} \cdot \overline{\Delta^{ss}\mathrm{FW}} + \overline{\gamma_{\mathrm{FW}}} \cdot \overline{P_{CO_2}} \cdot \frac{d\Delta^{ss}\mathrm{FW}}{dt} \quad (11)$$

The upper bar represents the local long-term mean of each variable. Equation (7) allows us to attribute the alterations in seasonal difference in P_{CO_2} to changes in SST, sDIC, sAlk, and FW. The three terms on the right-hand side of Eqs. 8 to 11 indicate the effects of the (i) changes in P_{CO_2} sensitivity, (ii) changes in P_{CO_2}, and (iii) changes in seasonal differences of each component on the trend of seasonal differences in P_{CO_2}, respectively. The sensitivity term (i) is zero for temperature but is relevant for sDIC and sAlk as this describes the impact of ocean acidification on these buffer factors. The P_{CO_2} term (ii) can be thought of as a mass effect, i.e., for the same drivers and for the same (relative) sensitivity, the seasonal amplitude increases in absolute terms, since the drivers act on a larger "mass" of CO_2. The third term (iii) describes the impact of the changes in the seasonality of drivers.

The spatial data are aggregated using a weighted averaging approach for regional analysis. Because our objective is to understand the contribution of the P_{CO_2} changes to the seasonality of air-sea CO_2 flux, the weights are based on the parameters that determine the flux, calculated as follows

$$\mathrm{Weights} = K_W \cdot S_{CO_2} \cdot (1 - [\mathrm{ice}]) \cdot \mathrm{area} \quad (12)$$

To identify the uncertainty of the regional average trends of each decomposed term, we use 95% confidence intervals derived from NCL software, which calculates linear regression coefficients with confidence estimates.

Time of emergence analysis

The time of emergence indicates the time when anthropogenic forcing starts to produce a statistically distinguishable signal from the background noise of natural and internal variability. To estimate the emergence time of anthropogenic signal on the changes in seasonal amplitude of air-sea CO_2 flux, a monthly flux dataset simulated from a large ensemble of Community Earth System Model 2 (CESM2-LE) is used (*45*). CESM2-LE consists of 100 members covering the period 1850–2100 under the Coupled Model Intercomparison Project version 6 (CMIP6) historical and Shared Socioeconomic Pathways (SSP) 370 future radiative forcing scenarios. In CESM2-LE, marine ecosystem dynamics and the carbon cycle are simulated using the Marine Biogeochemical Library (MARBL) (*72*). MARBL simulates two parallel carbonate systems. In both systems, the DIC and Alk tracers and associated quantities such as P_{CO_2} are diagnostically simulated but their atmospheric CO_2 boundary conditions are different; one uses time-varying level of atmospheric CO_2 concentration, and the other uses the preindustrial level of atmospheric CO_2 concentration (280 ppm) during the entire simulation period. Therefore, by comparing the simulated air-sea CO_2 fluxes in the two carbonate systems, we can separately estimate the contributions of natural and anthropogenic processes (i.e., ocean acidification) to the temporal variations of the air-sea CO_2 flux in the Southern Ocean during 1850–2100 [e.g., (*46*)].

To calculate the emergence time of the anthropogenically induced increasing trend of seasonal amplitude of air-sea CO_2 flux in the Southern Ocean, we first computed the differences between seasonal amplitudes of the flux induced by anthropogenic forcing and natural processes and then derived trends of the differences using a moving window of 20 years for each ensemble member. Here, the seasonal amplitude of the air-sea CO_2 flux is derived from the difference between the annual maximum and minimum of the detrended monthly flux. Then, the signal and noise are defined as the mean and SD of 100 ensemble member trends, respectively. The time of emergence is determined as the first year in which the magnitude of the signal exceeds 1.96 SD.

SUPPLEMENTARY MATERIALS

Supplementary material for this article is available at https://science.org/doi/10.1126/sciadv.abq0220

View/request a protocol for this paper from *Bio-protocol*.

REFERENCES AND NOTES

1. E. J. Dlugokencky, J. W. Mund, A. M. Crotwell, M. J. Crotwell, K. W. Thoning, Atmospheric carbon dioxide dry air mole fractions from the NOAA ESRL carbon cycle cooperative global air sampling network, 1968–2018, Version: 2019-07 (2019).
2. C. D. Keeling, J. F. S. Chin, T. P. Whorf, Increased activity of northern vegetation inferred from atmospheric CO_2 measurements. *Nature* **382**, 146–149 (1996).
3. J. T. Randerson, M. V. Thompson, T. J. Conway, I. Y. Fung, C. B. Field, The contribution of terrestrial sources and sinks to trends in the seasonal cycle of atmospheric carbon dioxide. *Global Biogeochem. Cycles* **11**, 535–560 (1997).
4. X. Zhang, K. R. Gurney, P. Rayner, D. Baker, Y.-P. Liu, Sensitivity of simulated CO_2 concentration to sub-annual variations in fossil fuel CO_2 emissions. *Atmos. Chem. Phys.* **16**, 1907–1918 (2016).
5. H. D. Graven, R. F. Keeling, S. C. Piper, P. K. Patra, B. B. Stephens, S. C. Wofsy, L. R. Welp, C. Sweeney, P. P. Tans, J. J. Kelley, B. C. Daube, E. A. Kort, G. W. Santoni, J. D. Bent, Enhanced seasonal exchange of CO_2 by northern ecosystems since 1960. *Science* **341**, 1085–1089 (2013).
6. M. Forkel, N. Carvalhais, C. Rödenbeck, R. Keeling, M. Heimann, K. Thonicke, S. Zaehle, M. Reichstein, Enhanced seasonal CO_2 exchange caused by amplified plant productivity in northern ecosystems. *Science* **351**, 696–699 (2016).
7. S. Piao, Z. Liu, Y. Wang, P. Ciais, Y. Yao, S. Peng, F. Chevallier, P. Friedlingstein, I. A. Janssens, J. Peñuelas, S. Sitch, T. Wang, On the causes of trends in the seasonal amplitude of atmospheric CO_2. *Glob. Chang. Biol.* **24**, 608–616 (2018).
8. A. Ito, M. Inatomi, D. N. Huntzinger, C. Schwalm, A. M. Michalak, R. Cook, A. W. King, J. Mao, Y. Wei, W. M. Post, W. Wang, M. A. Arain, S. Huang, D. J. Hayes, D. M. Ricciuto, X. Shi, M. Huang, H. Lei, H. Tian, C. Lu, J. Yang, B. Tao, A. Jain, B. Poulter, S. Peng, P. Ciais, J. B. Fisher, N. Parazoo, K. Schaefer, C. Peng, N. Zeng, F. Zhao, Decadal trends in the seasonal-cycle amplitude of terrestrial CO_2 exchange resulting from the ensemble of terrestrial biosphere models. *Tellus B Chem. Phys. Meteorol.* **68**, 28968 (2016).
9. L. R. Welp, P. K. Patra, C. Rödenbeck, R. Nemani, J. Bi, S. C. Piper, R. F. Keeling, Increasing summer net CO_2 uptake in high northern ecosystems inferred from atmospheric inversions and comparisons to remote-sensing NDVI. *Atmos. Chem. Phys.* **16**, 9047–9066 (2016).
10. A. Bastos, P. Ciais, F. Chevallier, C. Rödenbeck, A. P. Ballantyne, F. Maignan, Y. Yin, M. Fernández-Martínez, P. Friedlingstein, J. Peñuelas, S. L. Piao, S. Sitch, W. K. Smith, X. Wang, Z. Zhu, V. Haverd, E. Kato, A. K. Jain, S. Lienert, D. Lombardozzi, J. E. M. S. Nabel, P. Peylin, B. Poulter, D. Zhu, Contrasting effects of CO_2 fertilization, land-use change and warming on seasonal amplitude of Northern Hemisphere CO_2 exchange. *Atmos. Chem. Phys.* **19**, 12361–12375 (2019).
11. S.-J. Jeong, A. A. Bloom, D. Schimel, C. Sweeney, N. C. Parazoo, D. Medvigy, G. Schaepman-Strub, C. Zheng, C. R. Schwalm, D. N. Huntzinger, A. M. Michalak, C. E. Miller, Accelerating rates of Arctic carbon cycling revealed by long-term atmospheric CO_2 measurements. *Sci. Adv.* **4**, eaao1167 (2018).
12. J. M. Gray, S. Frolking, E. A. Kort, D. K. Ray, C. J. Kucharik, N. Ramankutty, M. A. Friedl, Direct human influence on atmospheric CO_2 seasonality from increased cropland productivity. *Nature* **515**, 398–401 (2014).
13. N. Zeng, F. Zhao, G. J. Collatz, E. Kalnay, R. J. Salawitch, T. O. West, L. Guanter, Agricultural green revolution as a driver of increasing atmospheric CO_2 seasonal amplitude. *Nature* **515**, 394–397 (2014).
14. C. D. Nevison, N. M. Mahowald, S. C. Doney, I. D. Lima, G. R. van der Werf, J. T. Randerson, D. F. Baker, P. Kasibhatla, G. A. McKinley, Contribution of ocean, fossil fuel, land biosphere, and biomass burning carbon fluxes to seasonal and interannual variability in atmospheric CO_2. *J. Geophys. Res. Biogeosci.* **113**, G01010 (2008).
15. I. Levin, T. Naegler, B. Kromer, M. Diehl, R. Francey, A. Gomez-Pelaez, P. Steele, D. Wagenbach, R. Weller, D. Worthy, Observations and modelling of the global distribution and long-term trend of atmospheric $^{14}CO_2$. *Tellus B Chem. Phys. Meteorol.* **62**, 26–46 (2010).
16. M. C. Long, B. B. Stephens, K. McKain, C. Sweeney, R. F. Keeling, E. A. Kort, E. J. Morgan, J. D. Bent, N. Chandra, F. Chevallier, R. Commane, B. C. Daube, P. B. Krummel, Z. Loh, I. T. Luijkx, D. Munro, P. Patra, W. Peters, M. Ramonet, C. Rödenbeck, A. Stavert, P. Tans, S. C. Wofsy, Strong Southern Ocean carbon uptake evident in airborne observations. *Science* **374**, 1275–1280 (2021).
17. C. Le Quéré, C. Rödenbeck, E. T. Buitenhuis, T. J. Conway, R. Langenfelds, A. Gomez, C. Labuschagne, M. Ramonet, T. Nakazawa, N. Metzl, N. Gillett, M. Heimann, Saturation of the Southern Ocean CO_2 sink due to recent climate change. *Science* **316**, 1735–1738 (2007).
18. T. DeVries, C. Le Quéré, O. Andrews, S. Berthet, J. Hauck, T. Ilyina, P. Landschützer, A. Lenton, I. D. Lima, M. Nowicki, J. Schwinger, R. Séférian, Decadal trends in the ocean carbon sink. *Proc. Natl. Acad. Sci. U.S.A.* **116**, 11646–11651 (2019).
19. P. Landschützer, N. Gruber, F. A. Haumann, C. Rödenbeck, D. C. E. Bakker, S. van Heuven, M. Hoppema, N. Metzl, C. Sweeney, T. Takahashi, B. Tilbrook, R. Wanninkhof, The reinvigoration of the Southern Ocean carbon sink. *Science* **349**, 1221–1224 (2015).
20. N. Gruber, P. Landschützer, N. S. Lovenduski, The variable Southern Ocean carbon sink. *Annu. Rev. Environ. Resour.* **11**, 159–186 (2019).
21. N. R. Bates, Y. M. Astor, M. J. Church, K. Currie, J. E. Dore, M. González-Dávila, L. Lorenzoni, F. Muller-Karger, J. Olafsson, J. M. Santana-Casiano, A time-series view of changing ocean chemistry due to ocean uptake of anthropogenic CO_2 and ocean acidification. *Oceanography* **27**, 126–141 (2014).
22. P. Landschützer, N. Gruber, D. C. E. Bakker, I. Stemmler, K. D. Six, Strengthening seasonal marine CO_2 variations due to increasing atmospheric CO_2. *Nat. Clim. Chang.* **8**, 146–150 (2018).
23. L. Kwiatkowski, J. C. Orr, Diverging seasonal extremes for ocean acidification during the twenty-first century. *Nat. Clim. Chang.* **8**, 141–145 (2018).
24. F. Chevallier, M. Fisher, P. Peylin, S. Serrar, P. Bousquet, F.-M. Bréon, A. Chédin, P. Ciais, Inferring CO_2 sources and sinks from satellite observations: Method and application to TOVS data. *J. Geophys. Res. Atmos.* **110**, D24309 (2005).
25. C. Rödenbeck, S. Zaehle, R. Keeling, M. Heimann, How does the terrestrial carbon exchange respond to inter-annual climatic variations? A quantification based on atmospheric CO_2 data. *Biogeosciences* **15**, 2481–2498 (2018).
26. J. G. Canadell, P. M. S. Monteiro, M. H. Costa, L. C. D. Cunha, P. M. Cox, A. V. Eliseev, S. Henson, M. Ishii, S. Jaccard, C. Koven, A. Lohila, P. K. Patra, S. Piao, S. Syampungani, S. Zaehle, K. Zickfeld, G. A. Alexandrov, G. Bala, L. Bopp, L. Boysen, L. Cao, N. Chandra, P. Ciais, S. N. Denisov, F. J. Dentener, H. Douville, A. Fay, P. Forster, B. Fox-Kemper, P. Friedlingstein, W. Fu, S. Fuss, V. Garçon, B. Gier, N. P. Gillett, L. Gregor, K. Haustein,

V. Haverd, J. He, H. T. Hewitt, F. M. Hoffman, T. Ilyina, R. Jackson, C. Jones, D. P. Keller, L. Kwiatkowski, R. D. Lamboll, X. Lan, C. Laufkötter, C. L. Quéré, A. Lenton, J. Lewis, S. Liddicoat, L. Lorenzoni, N. Lovenduski, A. H. Macdougall, S. Mathesius, D. H. Matthews, M. Meinshausen, I. I. Mokhov, V. Naik, Z. R. J. Nicholls, I. S. Nurhati, M. O'sullivan, G. Peters, J. Pongratz, B. Poulter, J.-B. Sallée, M. Saunois, E. A. G. Schuur, S. I. Seneviratne, A. Stavert, P. Suntharalingam, K. Tachiiri, J. Terhaar, R. Thompson, H. Tian, J. Turnbull, S. M. Vicente-Serrano, X. Wang, R. Wanninkhof, P. Williamson, V. Brovkin, R. A. Feely, A. D. Lebehot, in IPCC AR6 WGI, Final Government Distribution (2021), chapter 5; https://hal.archives-ouvertes.fr/hal-03336145.

27. J. Sarmiento, N. Gruber, *Ocean Biogeochemical Dynamics* (Princeton Univ. Press, 2006).
28. P. Landschützer, N. Gruber, D. C. E. Bakker, Decadal variations and trends of the global ocean carbon sink. *Global Biogeochem. Cycles* **30**, 1396–1417 (2016).
29. C. Rödenbeck, R. F. Keeling, D. C. E. Bakker, N. Metzl, A. Olsen, C. Sabine, M. Heimann, Global surface-ocean pCO_2 and sea–air CO_2 flux variability from an observation-driven ocean mixed-layer scheme. *Ocean Sci.* **9**, 193–216 (2013).
30. A. Denvil-Sommer, M. Gehlen, M. Vrac, C. Mejia, LSCE-FFNN-v1: A two-step neural network model for the reconstruction of surface ocean pCO_2 over the global ocean. *Geosci. Model Dev.* **12**, 2091–2105 (2019).
31. L. Gregor, A. D. Lebehot, S. Kok, P. M. S. Monteiro, A comparative assessment of the uncertainties of global surface ocean CO_2 estimates using a machine-learning ensemble (CSIR-ML6 version 2019a)—Have we hit the wall? *Geosci. Model Dev.* **12**, 5113–5136 (2019).
32. L. Gregor, N. Gruber, OceanSODA-ETHZ: A global gridded data set of the surface ocean carbonate system for seasonal to decadal studies of ocean acidification. *Earth Syst. Sci. Data* **13**, 777–808 (2021).
33. K. Oleson, D. Lawrence, G. Bonan, B. Drewniak, M. Huang, C. Koven, S. Levis, F. Li, W. Riley, Z. Subin, S. Swenson, P. Thornton, A. Bozbiyik, R. Fisher, C. Heald, E. Kluzek, J. Lamarque, P. Lawrence, L. Leung, W. Lipscomb, S. Muszala, D. Ricciuto, W. Sacks, J. Tang, Z. Yang, *Technical Description of Version 4.5 of the Community Land Model (CLM)* (National Center for Atmospheric Research, 2013).
34. T. Oda, S. Maksyutov, R. J. Andres, The Open-source Data Inventory for Anthropogenic CO_2, version 2016 (ODIAC2016): A global monthly fossil fuel CO_2 gridded emissions data product for tracer transport simulations and surface flux inversions. *Earth Syst. Sci. Data* **10**, 87–107 (2018).
35. R. Wang, S. Tao, P. Ciais, H. Z. Shen, Y. Huang, H. Chen, G. F. Shen, B. Wang, W. Li, Y. Y. Zhang, Y. Lu, D. Zhu, Y. C. Chen, X. P. Liu, W. T. Wang, X. L. Wang, W. X. Liu, B. G. Li, S. L. Piao, High-resolution mapping of combustion processes and implications for CO_2 emissions. *Atmos. Chem. Phys.* **13**, 5189–5203 (2013).
36. G. Murray-Tortarolo, A. Anav, P. Friedlingstein, S. Sitch, S. Piao, Z. Zhu, B. Poulter, S. Zaehle, A. Ahlström, M. Lomas, S. Levis, N. Viovy, N. Zeng, Evaluation of Land surface models in reproducing satellite-derived LAI over the high-latitude Northern hemisphere. Part I: Uncoupled DGVMs. *Remote Sens.* **5**, 4819–4838 (2013).
37. P. R. Halloran, Does atmospheric CO_2 seasonality play an important role in governing the air-sea flux of CO_2? *Biogeosciences* **9**, 2311–2323 (2012).
38. L. Merlivat, J. Boutin, D. Antoine, Roles of biological and physical processes in driving seasonal air–sea CO_2 flux in the Southern Ocean: New insights from CARIOCA pCO_2. *J. Mar. Syst.* **147**, 9–20 (2015).
39. T. Takahashi, J. Olafsson, J. G. Goddard, D. W. Chipman, S. C. Sutherland, Seasonal variation of CO_2 and nutrients in the high-latitude surface oceans: A comparative study. *Global Biogeochem. Cycles* **7**, 843–878 (1993).
40. A. Lenton, B. Tilbrook, R. M. Law, D. Bakker, S. C. Doney, N. Gruber, M. Ishii, M. Hoppema, N. S. Lovenduski, R. J. Matear, B. I. McNeil, N. Metzl, S. E. Mikaloff-Fletcher, P. M. S. Monteiro, C. Rödenbeck, C. Sweeney, T. Takahashi, Sea–air CO_2 fluxes in the Southern Ocean for the period 1990-2009. *Biogeosciences* **10**, 4037–4054 (2013).
41. L. Gregor, S. Kok, P. M. S. Monteiro, Interannual drivers of the seasonal cycle of CO_2 in the Southern Ocean. *Biogeosciences* **15**, 2361–2378 (2018).
42. K. B. Rodgers, J. L. Sarmiento, O. Aumont, C. Crevoisier, C. de Boyer Montégut, N. Metzl, A wintertime uptake window for anthropogenic CO_2 in the North Pacific. *Global Biogeochem. Cycles* **22**, GB2020 (2008).
43. N. S. Lovenduski, N. Gruber, S. C. Doney, Toward a mechanistic understanding of the decadal trends in the Southern Ocean carbon sink. *Global Biogeochem. Cycles* **22**, GB3016 (2008).
44. A. Lenton, R. J. Matear, Role of the Southern Annular Mode (SAM) in Southern Ocean CO_2 uptake. *Global Biogeochem. Cycles* **21**, GB2016 (2007).
45. K. B. Rodgers, S.-S. Lee, N. Rosenbloom, A. Timmermann, G. Danabasoglu, C. Deser, J. Edwards, J.-E. Kim, I. R. Simpson, K. Stein, M. F. Stuecker, R. Yamaguchi, T. Bódai, E.-S. Chung, L. Huang, W. M. Kim, J.-F. Lamarque, D. L. Lombardozzi, W. R. Wieder, S. G. Yeager, Ubiquity of human-induced changes in climate variability. *Earth Syst. Dynam.* **12**, 1393–1411 (2021).
46. K. M. Krumhardt, M. C. Long, K. Lindsay, M. N. Levy, Southern Ocean calcification controls the global distribution of alkalinity. *Global Biogeochem. Cycles* **34**, e2020GB006727 (2020).
47. M. A. Gallego, A. Timmermann, T. Friedrich, R. E. Zeebe, Drivers of future seasonal cycle changes in oceanic pCO_2. *Biogeosciences* **15**, 5315–5327 (2018).
48. S. Schlunegger, K. B. Rodgers, J. L. Sarmiento, T. L. Frölicher, J. P. Dunne, M. Ishii, R. Slater, Emergence of anthropogenic signals in the ocean carbon cycle. *Nat. Clim. Change* **9**, 719–725 (2019).
49. D. C. E. Bakker, B. Pfeil, C. S. Landa, N. Metzl, K. M. O'Brien, A. Olsen, K. Smith, C. Cosca, S. Harasawa, S. D. Jones, S. Nakaoka, Y. Nojiri, U. Schuster, T. Steinhoff, C. Sweeney, T. Takahashi, B. Tilbrook, C. Wada, R. Wanninkhof, S. R. Alin, C. F. Balestrini, L. Barbero, N. R. Bates, A. A. Bianchi, F. Bonou, J. Boutin, Y. Bozec, E. F. Burger, W.-J. Cai, R. D. Castle, L. Chen, M. Chierici, K. Currie, W. Evans, C. Featherstone, R. A. Feely, A. Fransson, C. Goyet, N. Greenwood, L. Gregor, S. Hankin, N. J. Hardman-Mountford, J. Harlay, J. Hauck, M. Hoppema, M. P. Humphreys, C. W. Hunt, B. Huss, J. S. P. Ibánhez, T. Johannessen, R. Keeling, V. Kitidis, A. Körtzinger, A. Kozyr, E. Krasakopoulou, A. Kuwata, P. Landschützer, S. K. Lauvset, N. Lefèvre, C. L. Monaco, A. Manke, J. T. Mathis, L. Merlivat, F. J. Millero, P. M. S. Monteiro, D. R. Munro, A. Murata, T. Newberger, A. M. Omar, T. Ono, K. Paterson, D. Pearce, D. Pierrot, L. L. Robbins, S. Saito, J. Salisbury, R. Schlitzer, B. Schneider, R. Schweitzer, R. Sieger, I. Skjelvan, K. F. Sullivan, S. C. Sutherland, A. J. Sutton, K. Tadokoro, M. Telszewski, M. Tuma, S. M. A. C. van Heuven, D. Vandemark, B. Ward, A. J. Watson, S. Xu, A multi-decade record of high-quality fCO_2 data in version 3 of the surface Ocean CO_2 atlas (SOCAT). *Earth Syst. Sci. Data* **8**, 383–413 (2016).
50. A. J. Fassbender, K. B. Rodgers, H. I. Palevsky, C. L. Sabine, Seasonal asymmetry in the evolution of surface Ocean pCO_2 and pH thermodynamic drivers and the influence on sea-air CO_2 flux. *Global Biogeochem. Cycles* **32**, 1476–1497 (2018).
51. D. J. Pilcher, S. R. Brody, L. Johnson, B. Bronselaer, Assessing the abilities of CMIP5 models to represent the seasonal cycle of surface ocean pCO_2. *J. Geophys. Res. Oceans* **120**, 4625–4637 (2015).
52. C. D. Nevison, M. Manizza, R. F. Keeling, B. B. Stephens, J. D. Bent, J. Dunne, T. Ilyina, M. Long, L. Resplandy, J. Tjiputra, S. Yukimoto, Evaluating CMIP5 ocean biogeochemistry and Southern Ocean carbon uptake using atmospheric potential oxygen: Present-day performance and future projection. *Geophys. Res. Lett.* **43**, 2077–2085 (2016).
53. L. Wang, J. Huang, Y. Luo, Z. Zhao, Narrowing the spread in CMIP5 model projections of air-sea CO_2 fluxes. *Sci. Rep.* **6**, 37548 (2016).
54. N. P. Mongwe, M. Vichi, P. M. S. Monteiro, The seasonal cycle of pCO_2 and CO_2 fluxes in the Southern Ocean: Diagnosing anomalies in CMIP5 Earth system models. *Biogeosciences* **15**, 2851–2872 (2018).
55. A. R. Gray, K. S. Johnson, S. M. Bushinsky, S. C. Riser, J. L. Russell, L. D. Talley, R. Wanninkhof, N. L. Williams, J. L. Sarmiento, Autonomous biogeochemical floats detect significant carbon dioxide outgassing in the high-latitude Southern Ocean. *Geophys. Res. Lett.* **45**, 9049–9057 (2018).
56. H. C. Bittig, T. L. Maurer, J. N. Plant, C. Schmechtig, A. P. S. Wong, H. Claustre, T. W. Trull, T. V. S. Udaya Bhaskar, E. Boss, G. Dall'Olmo, E. Organelli, A. Poteau, K. S. Johnson, C. Hanstein, E. Leymarie, S. Le Reste, S. C. Riser, A. R. Rupan, V. Taillandier, V. Thierry, X. Xing, A BGC-Argo guide: Planning, deployment, data handling and usage. *Front. Mar. Sci.* **6**, 502 (2019).
57. S. M. Bushinsky, P. Landschützer, C. Rödenbeck, A. R. Gray, D. Baker, M. R. Mazloff, L. Resplandy, K. S. Johnson, J. L. Sarmiento, Reassessing Southern Ocean air-sea CO_2 flux estimates with the addition of biogeochemical float observations. *Global Biogeochem. Cycles* **33**, 1370–1388 (2019).
58. B. I. McNeil, R. J. Matear, Southern Ocean acidification: A tipping point at 450-ppm atmospheric CO_2. *Proc. Natl. Acad. Sci. U.S.A.* **105**, 18860–18864 (2008).
59. L.-Q. Jiang, B. R. Carter, R. A. Feely, S. K. Lauvset, A. Olsen, Surface ocean pH and buffer capacity: Past, present and future. *Sci. Rep.* **9**, 18624 (2019).
60. B. B. Stephens, G. W. Brailsford, A. J. Gomez, K. Riedel, S. E. Mikaloff-Fletcher, S. Nichol, M. Manning, Analysis of a 39-year continuous atmospheric CO_2 record from Baring Head, New Zealand. *Biogeosciences* **10**, 2683–2697 (2013).
61. V. Cundari, T. Colombo, L. Ciattaglia, Thirteen years of atmospheric carbon dioxide measurements at Mt. Cimone station, Italy. *Il Nuovo Cimento C* **18**, 33–47 (1995).
62. K. W. Thoning, P. P. Tans, W. D. Komhyr, Atmospheric carbon dioxide at Mauna Loa Observatory: 2. Analysis of the NOAA GMCC data, 1974–1985. *J. Geophys. Res. Atmos.* **94**, 8549–8565 (1989).
63. R. Paternoster, R. Brame, P. Mazerolle, A. Piquero, Using the correct statistical test for the equality of regression coefficients. *Crim.* **36**, 859–866 (1998).
64. L. Gregor, A. Fay, SeaFlux: Air-sea CO_2 fluxes for surface pCO_2 data products using a standardised approach (2021.03) [K_w, S_{CO2}, [ice], and pCO_2^{atm}]. Zenodo (2021).
65. I. Bey, D. J. Jacob, R. M. Yantosca, J. A. Logan, B. D. Field, A. M. Fiore, Q. Li, H. Y. Liu, L. J. Mickley, M. G. Schultz, Global modeling of tropospheric chemistry with assimilated meteorology: Model description and evaluation. *J. Geophys. Res.* **106**, 23073–23095 (2001).
66. R. Gelaro, W. McCarty, M. J. Suárez, R. Todling, A. Molod, L. Takacs, C. A. Randles, A. Darmenov, M. G. Bosilovich, R. Reichle, K. Wargan, L. Coy, R. Cullather, C. Draper, S. Akella, V. Buchard, A. Conaty, A. M. da Silva, W. Gu, G.-K. Kim, R. Koster, R. Lucchesi,

D. Merkova, J. E. Nielsen, G. Partyka, S. Pawson, W. Putman, M. Rienecker, S. D. Schubert, M. Sienkiewicz, B. Zhao, The modern-era retrospective analysis for research and applications, Version 2 (MERRA-2). *J. Climate* **30**, 5419–5454 (2017).
67. J. Yun, S.-J. Jeong, C.-H. Ho, C.-E. Park, H. Park, J. Kim, Influence of winter precipitation on spring phenology in boreal forests. *Glob. Chang. Biol.* **24**, 5176–5187 (2018).
68. J. T. Randerson, G. R. Van Der Werf, L. Giglio, G. J. Collatz, P. S. Kasibhatla, Global Fire Emissions Database, Version 4 (GFEDv4), ORNL DAAC, Oak Ridge, Tennessee, USA (2015).
69. S. Good, E. Fiedler, C. Mao, M. J. Martin, A. Maycock, R. Reid, J. Roberts-Jones, T. Searle, J. Waters, J. While, M. Worsfold, The Current configuration of the OSTIA system for operational production of foundation sea surface temperature and ice concentration analyses. *Remote Sens.* **12**, 720 (2020).
70. S. A. Good, M. J. Martin, N. A. Rayner, EN4: Quality controlled ocean temperature and salinity profiles and monthly objective analyses with uncertainty estimates. *J. Geophys. Res. Oceans* **118**, 6704–6716 (2013).
71. M. P. Humphreys, E. R. Lewis, J. D. Sharp, D. Pierrot, PyCO2SYS v1.8: Marine carbonate system calculations in Python. *Geosci. Model Dev.* **15**, 15–43 (2022).
72. M. C. Long, J. K. Moore, K. Lindsay, M. Levy, S. C. Doney, J. Y. Luo, K. M. Krumhardt, R. T. Letscher, G. Maxwell, Z. T. Sylvester, Simulations with the Marine Biogeochemistry Library (MARBL). *J. Adv. Model. Earth Syst.* **13**, e2021MS002647 (2021).

Acknowledgments: We thank observation data provider of atmospheric CO_2 at NOAA/ESRL, ECCC, FMI, JMA, NIWA, IAFMS, RSE, SAIPF, and UBAG and of inverse modeling outputs at CAMS and Jena CarboScope. We also appreciate all of the data providers of the datasets used in GEOS-Chem model simulations and Pco_2 decomposition analysis. Especially, we thank all research groups involved in SOCAT and SOCOM projects contributing to make global Pco_2 and air-sea CO_2 flux datasets and E.U. Copernicus Marine Service Information for providing the CMEMS Pco_2 datasets. **Funding:** This study is supported by Korea Environment Industry &Technology Institute (KEITI) through "Climate Change R&D Project for New Climate Regime," funded by Korea Ministry of Environment (MOE) (2022003560006). N.G. and L.G. acknowledge funding from ETH Zürich and the European Commission through the COMFORT (grant no. 820989) and the 4C projects (grant no. 821003). **Author contributions:** S.J. designed this study, and J.Y. performed most of the analyses. N.G. and L.G. conceived the decomposition analysis of the oceanic Pco_2, with L.G. computing it. C.-H.H., N.G., S.P., P.C., D.S., and E.Y.K. reviewed and provided input to the manuscript. J.Y. led the writing with input from all coauthors, especially N.G. **Competing interests:** The authors declare that they have no competing interests. **Data and materials availability:** All data needed to evaluate the conclusions in the paper are present in the paper and/or the Supplementary Materials. Atmospheric CO_2 measurement datasets are available at https://gaw.kishou.go.jp/. The inverse modeling results from the CAMS are publicly available at https://apps.ecmwf.int/datasets/data/cams-ghg-inversions/. The inverse modeling results and Pco_2-based products from Jena CarboScope are available at www.bgc-jena.mpg.de/CarboScope/. Pco_2-based products from OceanSODA-ETHZ, MPI-SOMFFN, CSIR-ML6, and CMEMS-FFNN are available at https://doi.org/10.25921/m5wx-ja34, www.ncei.noaa.gov/data/oceans/ncei/ocads/data/0160558/, https://doi.org/10.6084/m9.figshare.12652100.v9, and https://doi.org/10.48670/moi-00047, respectively. The CESM2-LE simulation results are available at https://doi.org/10.26024/kgmp-c556. The results of CLM4.5-CN and GEOS-Chem model simulations and codes required for linear decomposition analysis of Pco_2 are available on Zenodo (https://doi.org/10.5281/zenodo.6983938 and https://doi.org/10.5281/zenodo.6983828, respectively).

Submitted 13 March 2022
Accepted 25 August 2022
Published 12 October 2022
10.1126/sciadv.abq0220